Validating optical emission spectroscopy as a diagnostic of microwave activated $CH_4/Ar/H_2$ plasmas used for diamond chemical vapor deposition

Jie Ma,[1] Michael N. R. Ashfold,[1,a)] and Yuri A. Mankelevich[2]
[1]*School of Chemistry, University of Bristol, Bristol BS8 1TS, United Kingdom*
[2]*Skobel'tsyn Institute of Nuclear Physics, Moscow State University, Vorob'evy gory, Moscow 119991 Russia*

(Received 31 July 2008; accepted 1 January 2009; published online 18 February 2009)

Spatially resolved optical emission spectroscopy (OES) has been used to investigate the gas phase chemistry and composition in a microwave activated $CH_4/Ar/H_2$ plasma operating at moderate power densities ($\sim$30 W cm^{-3}) and pressures ($\leq$175 Torr) during chemical vapor deposition of polycrystalline diamond. Several tracer species are monitored in order to gain information about the plasma. Relative concentrations of ground state H ($n=1$) atoms have been determined by actinometry, and the validity of this method have been demonstrated for the present experimental conditions. Electronically excited H ($n=3$ and 4) atoms, Ar ($4p$) atoms, and C_2 and CH radicals have been studied also, by monitoring their emissions as functions of process parameters (Ar and CH_4 flow rates, input power, and pressure) and of distance above the substrate. These various species exhibit distinctive behaviors, reflecting their different formation mechanisms. Relative trends identified by OES are found to be in very good agreement with those revealed by complementary absolute absorption measurements (using cavity ring down spectroscopy) and with the results of complementary two-dimensional modeling of the plasma chemistry prevailing within this reactor. © *2009 American Institute of Physics*. [DOI: 10.1063/1.3078032]

I. INTRODUCTION

Optical emission spectroscopy (OES) is a sensitive and noninvasive technique for "fingerprinting" specific (emitting) species in plasmas; indeed, it is arguably the simplest and most straightforward means of investigating the behavior of such species in the plasma. The interpretation of OES data is complicated by the need for a proper understanding of the various species excitation and de-excitation processes but, as shown below, careful analysis can yield quantitative information.

OES was one of the first spectroscopic methods used to diagnose microwave (MW) plasmas used for diamond chemical vapor deposition (CVD). Zhu *et al.*[1] studied the influence of different rare gases on diamond deposition from MW activated CH_4/rare gas/H_2 mixtures. C_2, H Balmer-α, and H Balmer-β emission intensities were compared with and without the rare gas. Addition of rare gas had an obvious influence on the generation and excitation of these tracer species (through energy and/or charge transfer from the excited and/or ionic states of the rare gas), but the available spectral resolution was insufficient to allow determination of the gas temperature, T_{gas}. Also, this particular plasma operated at low input powers ($P=310$ W) and a pressure $p=90$ Torr; the deduced chemistry is not necessarily transferable to the higher powers (several kilowatts) and pressures relevant for most contemporary MW reactors. Gicquel *et al.*[2,3] subsequently reported higher resolution measurements of H_α emission from a MW plasma operating at, typically, $P=600$ W and $p=20$ Torr. The gas temperature deduced from the H_α Doppler linewidth measurements agreed well with that obtained from two-photon absorption laser induced fluorescence (TALIF) studies of H ($n=1$) atoms and with the rotational temperature of the ground state H_2 molecules determined by coherent anti-Stokes–Raman spectroscopy. The same group also pioneered the use of the actinometry method for measuring relative concentrations of H ($n=1$) atoms in MW plasma enhanced diamond CVD, under a range of process conditions.[4,5] Lang *et al.*[6] reported high resolution OES studies of the H_2 Fulcher (0,0) Q branch and of the H_α transition in a MW plasma operating at $400<P<880$ W and $38<p<75$ Torr. The gas temperature could thus be estimated from the H_2 rotational temperature, and from the Doppler broadening of the H_α line at 656.3 nm and the H_2 Fulcher (0,0) $Q1$ line at 601.83 nm. These workers concluded that the H_2 Doppler linewidth was the most reliable measure of T_{gas}, and that the H_α linewidth and H_2 rotational temperature, respectively, provided over- and underestimates of the gas temperature. Actinometry was also used in this study to determine relative concentrations of H ($n=1$) atoms.

Goyette *et al.*[7] used both OES and white-light absorption spectroscopy to monitor C_2 radicals in an Ar-rich (>90%) MW activated $CH_4/Ar/H_2$ plasma used for depositing nanocrystalline diamond. The measured $C_2(d\,^3\Pi_g - a\,^3\Pi_u)$ Swan band emission intensities were found to correlate well with the $C_2(a)$ densities determined by absorption spectroscopy, for a range of process conditions (varying total pressure, carbon and H_2 mole fractions, and the substrate temperature). John *et al.*[8] also found a linear relationship between C_2 Swan band emission intensities and the C_2 column densities [measured by cavity ring down spectroscopy (CRDS)] in a MW activated $CH_4/Ar/H_2$ plasma operating under Ar-rich condi-

a)Author to whom correspondence should be addressed. Tel.: (117)-9288312/3. FAX: (117)-9250612. Electronic mail: mike.ashfold@bris.ac.uk.

tions, although the spectra also show strong CN radical emissions (hinting at some air contamination of the process gas mixture).

The OES studies summarized above generally involved MW plasmas operating at relatively low input powers ($P < 1$ kW) and/or pressures ($p < 100$ Torr), or the use of Ar-rich gas mixtures. The correlation between OES and absorption measurements in more traditional H_2-rich gas mixtures and under (higher) P and p conditions more representative of contemporary MW-CVD reactors thus merits further study. Here we report comparative, spatially resolved relative studies of C_2, CH, H ($n=2$), H_2, and Ar species in emission (by OES), and absolute column densities of C_2, CH, H ($n=2$) species in absorption (by CRDS), as functions of process conditions, at $P \leq 1.5$ kW and $p \leq 175$ Torr for $CH_4/H_2/Ar$ gas mixtures typical of those used in polycrystalline diamond CVD. Such increased input powers and pressures result in a higher average MW power density, Q, and consequent increases in T_{gas}, the electron density (n_e), and/or the electron temperature (T_e). Both thermally driven and electron-driven chemistry will thus be enhanced, leading to increased radical generation and, potentially, improvements in the rate of diamond CVD and/or the quality of the deposited material. The present study provides additional insights into the behaviors of electrons and (via actinometry) the H ($n=1$) atoms as functions of different plasma parameters. As such, it complements other recent studies of MW activated $CH_4/Ar/H_2$ gas mixtures in this same reactor which emphasized $C_1H_y \leftrightarrow C_2H_x$ species interconversion[9] and aspects of the radical chemistry prevailing in the plasma ball[10] and provides a further test and validation of the reported two-dimensional (2D) reactor modeling.[11]

II. EXPERIMENTAL

Details of the custom-designed MW reactor (2 kW, 2.45 GHz Muegge power supply and generator) have been presented previously.[9,12] MW power is delivered along the rectangular waveguide, at the exit of which it is converted into the TM_{01} mode and coupled into the cylindrical chamber. The chamber is divided into two parts by a centrally mounted quartz window. The lower chamber is vacuum sealed and contains the plasma. The premixed $CH_4/Ar/H_2$ process gas mixture is fed through two diametrically opposed inlets located beneath the window and is exhausted through the base plate. The MW radiation partially ionizes and dissociates the gas mixture, "active" species are produced, some of which react on the molybdenum substrate (3 cm diameter) to form a polycrystalline diamond film. For future reference, the "base" discharge conditions are as follows: total pressure $p=150$ Torr, input power $P=1.5$ kW, and flow rates $F(Ar)=40$ SCCM (SCCM denotes cubic centimeter per minute at STP), $F(CH_4)=25$ SCCM, and $F(H_2)=500$ SCCM. When investigating the effects of varying $F(Ar)$ and/or $F(CH_4)$, any variation away from the base condition is compensated by a corresponding adjustment in $F(H_2)$ so as to ensure that the total flow is always 565 SCCM.

The two different arrangements used in the present studies are shown in Fig. 1, while the setup for the CRDS measurements (and the extraction of spatially resolved, species specific, line integrated absorbances, and hence column densities) has been described elsewhere.[10] Overview OES data from a localized volume somewhat below the center of the luminous plasma ball was obtained by viewing transverse to the laser probe axis, through an ~9 mm diameter aperture located behind a glass view port that was vacuum sealed to a flange mounted on the reactor wall. Emission passing through this aperture was focused (glass lens) onto one end of a quartz multicore optical fiber (Oriel), as per the arrangement labeled optical fiber I (8) in Fig. 1. Light exiting the fiber (in the form of a vertical stripe) is dispersed through a fast monochromator equipped with a charge coupled device (CCD) strip detector (Oriel Instaspec IV, 600 lines mm^{-1} ruled grating) that provides a spectral resolution better than 1 nm. The length of the detector allows simultaneous sampling of a 300 nm portion of the OES spectrum so, in the present experiments, the grating position is adjusted manually to allow collection of "long" (~540–840 nm) and "short" (~380–680 nm) wavelength scans. The CCD detector was cooled to 10 °C to reduce its background count rate. Typical CCD exposure times for measurements of the plasma emission (and the background, recorded with the plasma emission blocked) were 100 ms, and the data averaged 2000 times; the displayed spectra are measured spectra after subtraction of the background.

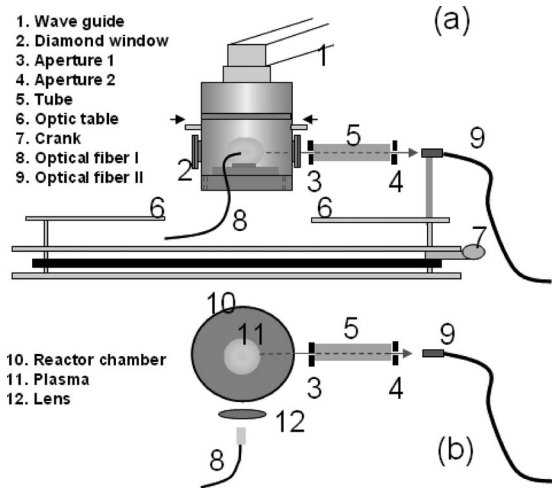

FIG. 1. Schematic of the experimental arrangement [(a) side and (b) top views] illustrating the optical setups for transverse and longitudinal (spatially resolved) OES studies (labeled optical fibers I and II).

Spatially resolved OES experiments involved viewing along the axis designed for laser diagnosis, through one of the diamond windows. The quartz fiber was positioned so as to view the plasma ball behind a light-confining assembly comprising two 1–2 mm diameter apertures (3, 4) and a light-tight spacer tube (5) on the movable optical table (6)—illustrated as optical fiber II (9) in Fig. 1. This arrangement allowed vertical profiling with a spatial resolution of ~2 mm over a height of ~25 mm,[13] but the much reduced viewing solid angle (*cf* optical fiber I position) required the use of much longer exposure times (typically 60 s), with 3 averages per spectrum. The emission lines used to monitor

TABLE I. Species, transition wavelengths (λ), upper and lower level assignments, and energies (E) for the tracers monitored in the present OES studies of MW activated $CH_4/Ar/H_2$ plasmas.

Species	λ (nm)	Upper level	E (eV)	Lower level	E (eV)
CH	431.4	$A\ ^2\Delta$	(2.88)	$X\ ^2\Pi$	(0.00)
H (n=4)	486.1(H_β)	n=4	(12.75)	n=2	(10.20)
C_2	516.5	$d\ ^3\Pi_g$	(2.41)	$a\ ^3\Pi_u$	(0.09)
H_2	602.1	$3p\ ^3\Sigma_u^+$	(13.28)	$2s\ ^3\Sigma_g^+$	(11.84)
H (n=3)	656.3(H_α)	n=3	(12.10)	n=2	(10.20)
Ar ($4p$)	750.4	$3s^23p^5[^2P^o_{1/2}]4p$	(13.52)	$3s^23p^5[^2P^o_{1/2}]4s$	(11.86)

the various tracer species, and their assignments, are summarized in Table I.

III. RESULTS AND DISCUSSION

A. H actinometry

H atoms play a number of vital roles in the diamond CVD process,[14,15] so understanding the H atom chemistry is of paramount importance. Traditional OES methods (i.e., monitoring H atom emissions) only provide direct information about electronically excited H atoms. A number of laser spectroscopy methods have been applied to the detection of ground state H atoms, however. For example, resonance enhanced multiphoton ionization spectroscopy has been used to determine relative concentrations of H (n=1) atoms in hot-filament activated gas mixtures,[16,17] but this technique is not suitable for use in a MW reactor. TALIF methods have also been used to probe H (n=1) atoms—both in a HFCVD reactor and in rf discharges,[18–21] but very careful calibration experiments are required in order to convert measured TALIF signals into absolute H (n=1) number densities. Absorption spectroscopy has fewer such calibration difficulties, but the direct measurement of H (n=1) atoms in absorption is often complicated by saturation effects and is limited by the availability of suitable vacuum ultraviolet light sources. Actinometry may therefore be one of the best available choices for monitoring H (n=1) atoms in a MWCVD reactor.

The principles underpinning actinometry and its use as a plasma diagnostic have been thoroughly described elsewhere.[4,5,22–25] Briefly, the method involves the addition of a small, known, amount of an inert tracer species (e.g., Ar, as here)—the actinometer—to the gaseous medium of interest. Then, by comparing the intensities of specific emissions of the actinometer and of the species (X) of interest, the concentration of the latter can be deduced from the relation

$$[X]/[\mathrm{act}] = kI_X/I_{\mathrm{act}}, \quad (1)$$

where $[X]$ and [act] represent the respective concentrations and I_X and I_{act} are their relative emission intensities.

Gicquel *et al.*[5] discussed a number of conditions that must be satisfied in order to ensure the validity of Eq. (1). First, the addition of the actinometer should not perturb the plasma. This is not an issue in the present work, since the Ar is already present as a required constituent of the plasma. Second, the excited states of X and of the actinometer responsible for the monitored emissions in Eq. (1) should be populated by direct electron impact excitation of the respective ground states. Third, the excitation cross sections for these two species should have similar energy thresholds and profiles. The same authors have also specifically addressed the validity of using actinometry methods to determine the relative concentration of H (n=1) atoms in a MW plasma used for diamond CVD, typically at $p \sim 20$ Torr, $P \sim 600$ W, and $Q \sim 9$ W cm^{-3}.[5,26] Although these pressures and powers are much lower than the base conditions of interest in the present work ($p \sim 150$ Torr, $P \sim 1.5$ kW), their analysis is highly instructive. Thus a similar procedure is followed here in order to assess the applicability of actinometry under the present experimental conditions.

Figure 2 shows a typical spectrum for H actinometry, with the spectrometer set to transmit the long wavelength range. The H_α transition and three of the stronger Ar emission lines are readily identifiable. Following Gicquel *et al.*,[26] we focus our attention on the H_α and Ar 750.4 nm emission lines, given the similar thresholds and T_e dependent electron impact excitation cross sections for forming H (n=3) and Ar ($3s^23p^5[^2P^o_{1/2}]4p$)—henceforth Ar ($4p$)—atoms. The main processes involved in the production and loss of H (n=3) and Ar ($4p$) population are summarized in Tables II and III. Some of these processes [e.g., those involving H (n=2) and H (n=3)] are included explicitly in the full plasma chemical mechanism,[11] while processes involving highly excited argon atoms are treated as in Ref. 26, and the monitored Ar ($4p$) atoms are assumed to behave similarly to the Ar^{**} species (i.e., the Ar ($4s$) resonant states) described in Ref. 11.

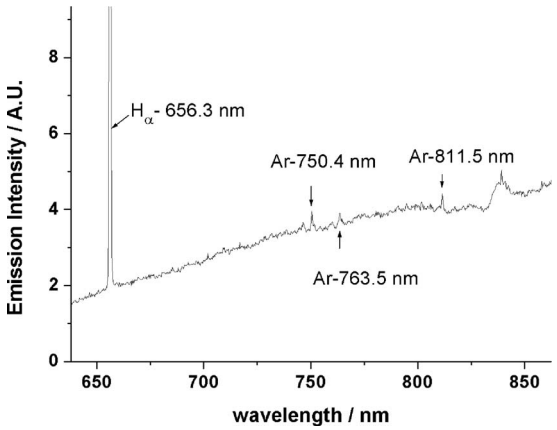

FIG. 2. Optical emission spectrum in the wavelength range 640–860 nm measured under base conditions with optical fiber I. Emissions attributable to H (n=3) and Ar ($4p$) atoms are indicated.

TABLE II. Main processes involved in the production and loss of H ($n=3$) atoms.

Process	Reaction		Rate constant
Production			
Electron impact excitation from ground state	$H(n=1)+e \rightarrow H(n=3)+e$	(R1)	$K_e^{H_\alpha}$
Consumption			
Radiative decay	$H(n=3) \rightarrow H(n=2)+h\nu$	(R2)	A_{32}
Radiative decay	$H(n=3) \rightarrow H(n=1)+h\nu$	(R3)	A_{31}
Quenching	$H(n=3)+M \rightarrow H(n=1)+M^*$	(R4)	$K_Q^{H_\alpha}$

Balancing the production and loss equations for H ($n=3$) and Ar ($4p$) atoms, as described in Tables II and III, leads to the following expression for the relative concentrations of ground state H ($n=1$) atoms in the present experiments:

$$[H(n=1)] \sim [Ar] I_{656}/I_{750}, \tag{2}$$

where I_{656} and I_{750} are, respectively, the H_α and Ar ($4p$) emission intensities. The derivation of Eq. (2) is summarized in the Appendix. The relative H_2 dissociation fraction f_{rel} can also be obtained using the relationship

$$f_D = \frac{[H(n=1)]/2}{[H(n=1)]/2+[H_2]} \approx \frac{[H(n=1)]}{[Ar]} \frac{X_{Ar}^0 b_{Ar}}{2X_{H_2}^0}$$

$$\sim \frac{I_{656}}{I_{750}} \frac{X_{Ar}^0}{2X_{H_2}^0} = f_{rel}, \tag{3}$$

where f_D is the absolute H_2 dissociation fraction, $[H_2]$ is the H_2 number density, and $X_{H_2}^0$ and X_{Ar}^0 are the mole fractions of H_2 and Ar in the input gas stream. b_{Ar} is a factor that describes the extent to which the initial argon fraction is reduced in the hot plasma region as a result of thermodiffusional transfer—calculated to be in the range ~0.38–0.5 in the present experiments. The derivations of Eqs. (2) and (3) are summarized in the Appendix.

B. H ($n=1$), H ($n=3$), and Ar ($4p$) number densities as functions of process parameters

Figure 3 shows the variations in measured Ar 750.4 nm and H_α emission intensities, and in the relative concentration of H ($n=1$) atoms as determined by actinometry, as functions of process conditions (i.e., $F(Ar)$, $F(CH_4)$, P, and p). For ease of display, the two emission intensities and the H ($n=1$) concentrations have each been scaled such that the maximum value in each data set is unity. The H_2 dissociation fraction, f_D, calculated using Eq. (3) is also shown (right hand axis) in each panel of the figure; the derived values have been placed on an absolute scale by reference to the calculated f_D value under base conditions.

These data are discussed in turn. The normalized Ar 750.4 nm emission scales near linearly with $F(Ar)$ [Fig. 3(a)], but neither the normalized H_α emission intensity nor the H ($n=1$) concentration (or the H_2 dissociation fraction f_D) changes significantly as $F(Ar)$ is increased from 0 to 50 SCCM—thereby confirming that the small amounts of Ar used cause minimal perturbation of the plasma. Addition of just 5 SCCM of CH_4 to the Ar/H_2 plasma causes an approximately twofold increase in both the Ar 750.4 nm and H_α emissions [Fig. 3(b)], but increasing $F(CH_4)$ further results in a gradual decline in both emission intensities. Such behavior is reminiscent of that found for the H ($n=2$) column densities determined by CRDS in this same reactor.[10] Figure 3(b) also shows that neither the H ($n=1$) relative concentration nor the H_2 dissociation fraction derived by actinometry is sensitive to $F(CH_4)$, so we must look elsewhere to account for the observed variations in the H ($n=2$) column densities and in the H_α emissions. Given the chemical inertness of Ar, it is most logical to attribute the rise [at low $F(CH_4)$] and subsequent decline in excited H and Ar atom densities to changes in the electron distribution caused by CH_4 addition.

The 2D modeling confirms such expectations.[11] The dominant ion in the plasma switches from H_3^+ to $C_2H_3^+$ and $C_2H_2^+$ upon adding just 5 SCCM of CH_4 to a pre-existing Ar/H_2 plasma. These hydrocarbon ions have much lower mobility than H_3^+; the plasma volume therefore shrinks (e.g., the plasma radius r_{pl} in the 2D model calculations declines from 3.4 to 3.0 cm) and the power density increases—leading to an increase in both the electron density and the electron temperature. For example, n_e is predicted to increase from 1.91×10^{11} to 2.54×10^{11} cm^{-3}, and T_e from 1.26 to 1.32 eV, upon introducing just 5 SCCM of CH_4 into an Ar/H_2 plasma operating under otherwise base conditions.

TABLE III. Main processes involved in the production and loss of Ar ($4p$) atoms.

Reaction name	Reaction		Rate constant
Production			
Electron impact excitation from ground state	$Ar(3p)+e \rightarrow Ar(4p)+e$	(R5)	$K_e^{Ar^*}$
Consumption			
Radiative de-excitation	$Ar(4p) \rightarrow Ar(4s)+h\nu$	(R6)	A_{44}
Quenching	$Ar(4p)+M \rightarrow Ar(3p,4s)+M^*$	(R7)	$K_Q^{Ar^*}$

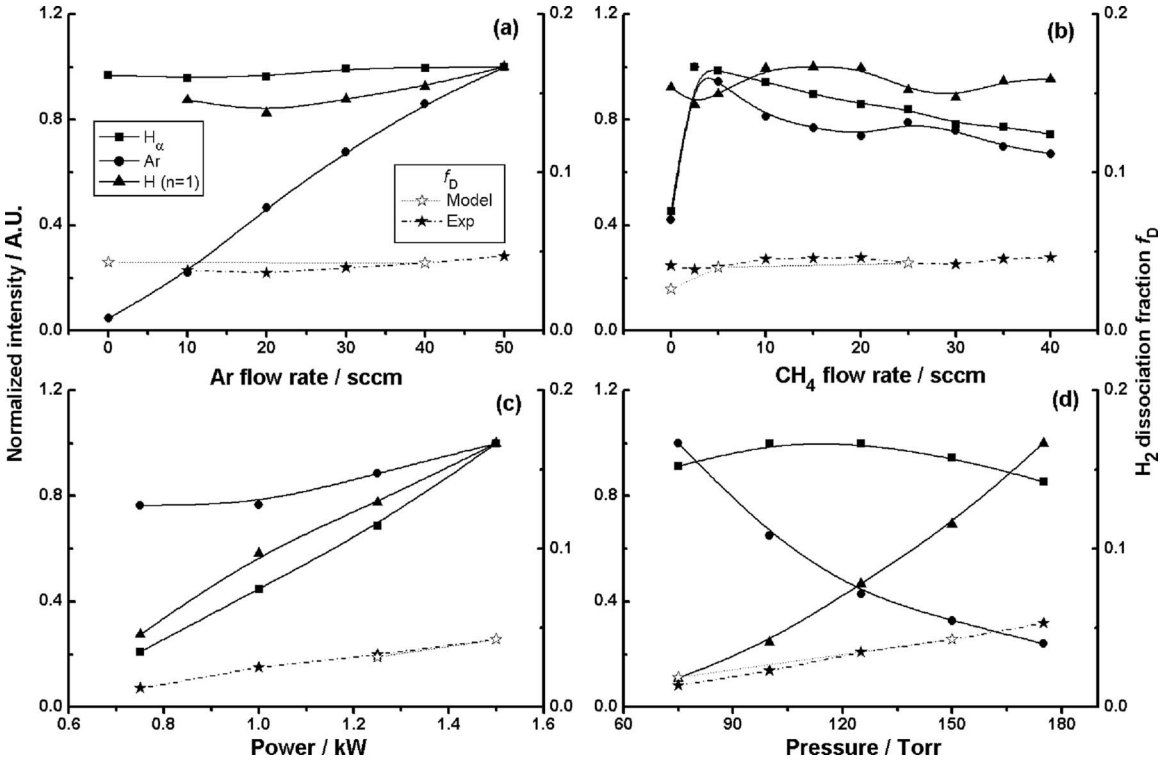

FIG. 3. Normalized relative Ar 750.4 nm and H_α emission intensities and H ($n=1$) densities determined by actinometry (left hand axis) and H_2 dissociation fraction (right hand axis), plotted as functions of (a) $F(Ar)$, (b) $F(CH_4)$, (c) P, and (d) p. The variations in normalized emission intensities from one spectrum to another recorded under the same process conditions are smaller than the displayed data points.

Increasing $F(CH_4)$ to 25 SCCM serves to reinforce the dominance of electron impact ionization of C_2H_2 (relative to the H_2 and H ionization processes) and shifts the $C_2H_3^+/C_2H_2^+$ balance more toward the latter [from $[C_2H_3^+]/[C_2H_2^+]\sim 4$ at $F(CH_4)=5$ SCCM to $[C_2H_3^+]/[C_2H_2^+]\sim 1$ at $F(CH_4)=25$ SCCM],[11] but the plasma volume and power density are relatively insensitive to such changes. C_2H_2 has a comparatively low ionization threshold ($\sim$11.4 eV), and increasing the C_2H_2 concentration leads to a decrease in T_e and an increase in n_e. For example, at base conditions [i.e., $F(CH_4)=25$ SCCM], the calculated value of n_e has risen to 2.70×10^{11} cm^{-3}, while T_e has declined to 1.28 eV. Since the H ($n\geq 2$) and Ar excited state generation rates scale near exponentially with T_e, this (small) drop in T_e suffices to account for the observed decline in excited state emission intensities at higher $F(CH_4)$.

Figure 3(c) illustrates the different power dependences of the normalized Ar and H_α emission intensities; the latter increase much more rapidly with increasing P. The relative concentration of H ($n=1$) atoms and the H_2 dissociation fraction derived by actinometry both show near-linear dependences on P, reflecting the increase in the average power density Q and the predominant use of this power in gas heating and H_2 dissociation.[11] Changes in p also have very different effects on the normalized Ar and H_α emissions. As Fig. 3(d) shows, the H_α intensity is relatively insensitive to an $\sim$2.3-fold increase in p (from 75 to 175 Torr) whereas the Ar 750.4 nm emission falls by a factor of $\sim$5. This latter observation reflects the decline in T_e that accompanies this increase in p. From actinometry, we therefore deduce that the normalized H ($n=1$) density increases almost tenfold over this p range, and that the H_2 dissociation fraction is three times larger at 175 Torr than at 75 Torr. Once again, these observations serve to confirm the model predictions: H ($n=1$) production in the present MW reactor operating under base conditions is dominated by thermal (rather than electron impact) dissociation of H_2. Careful inspection of Fig. 3(d) hints at a maximum in the H_α emission intensity at $p\sim 120$ Torr. Such a trend can be understood by recalling that the H_α emission arises as a result of electron impact excitation of H ($n=1$) atoms (Table II). Raising p thus has both a positive [by increasing the H ($n=1$) density] and a negative (by decreasing T_e) impact on the H ($n=3$) production rate, and the competition between these two effects leads to the observed p-dependence.

The corresponding variations in f_D predicted by the 2D reactor modeling are also included in the various panels of Fig. 3. These, too, are seen to agree well with the experimental observations, apart from the case of the $F(CH_4)=0$ data point in Fig. 3(b).

C. H ($n=3$), H ($n=4$), CH(A), and $C_2(d)$ number densities as functions of process parameters

As Fig. 4 shows, emissions attributable to electronically excited CH(A) and $C_2(d)$ radicals, H_2 molecules, and H [$n=3$, 4, 5, and (weakly) 6] atoms are identifiable in spectra obtained by monitoring the shorter wavelength range 390–670 nm. The dominant production and loss channels for electronically excited H atoms are, respectively, electron impact excitation of H ($n=1$) atoms and radiative decay. [Electron impact excitation rates are predicted to be more than ten

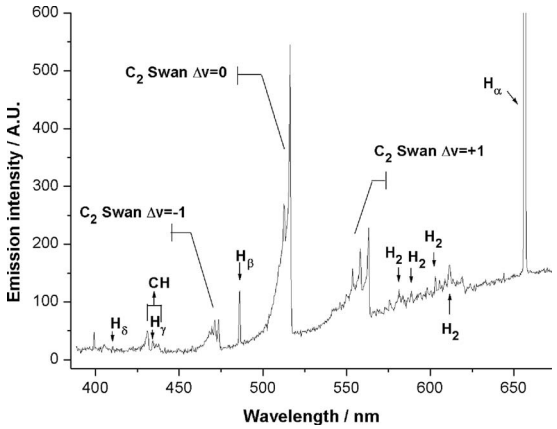

FIG. 4. Optical emission spectrum in the wavelength range 390–670 nm measured with optical fiber I with $F(CH_4)=40$ SCCM and all other parameters set to the base condition. Emission features attributable to electronic excited H atoms and to $C_2(d)$ and $CH(A)$ radicals are indicated.

times faster than the rates of Penning excitation (by excited Ar atoms) or electron impact induced dissociative excitation, and the radiative loss rates are similarly predicted to be at least an order of magnitude larger than the various competing quenching processes.[11]] In principle, therefore, the ratio of the H_β to H_α emission intensities $[I(H_\beta)/I(H_\alpha)]$ can be used as an indicator of T_e in the viewed region of the plasma.

Figure 5 shows how the intensities of emissions from $CH(A)$ and $C_2(d)$ radicals (at 431.4 and 516.5 nm, respectively) and H ($n=3$ and 4) atoms (at 656.3 and 486.1 nm), together with the $I(H_\beta)/I(H_\alpha)$ ratio, vary with process conditions [i.e., $F(Ar)$, $F(CH_4)$, P, and p]. Increasing $F(Ar)$ from 0 to 50 SCCM [Fig. 5(a)] has no discernible effect on the normalized H_α and H_β emissions, nor on the $I(H_\beta)/I(H_\alpha)$ ratio—illustrating, once again, that such small additions of Ar have little influence on the plasma or the electron characteristics (i.e., n_e and T_e). The normalized C_2 and CH emissions, in contrast, both increase with increasing Ar flow rate in the range $0<F(Ar)<50$ SCCM. As in the companion CRDS studies,[10] these increases can be attributed to changes in the thermal chemistry. Any increase in $F(Ar)$ in the present experiments is balanced by a compensatory reduction in $F(H_2)$ so as to maintain constant F_{total}. As a result, T_{gas} and the C/H ratio in the feed gas mixture both increase sufficiently over the range $0<F(Ar)<50$ SCCM to cause a measurable rise in the $CH(X)$ and $C_2(a)$ radical densities[10] and in the related excited state emissions.

Figure 5(b) shows the effect of $F(CH_4)$ on the various species emission intensities and the $I(H_\beta)/I(H_\alpha)$ ratios. The observed variations in the H_α and H_β emissions upon increasing $F(CH_4)$ reflect changes in the electron characteristics, although the near constancy of the $I(H_\beta)/I(H_\alpha)$ ratio implies that T_e does not vary significantly. The model calculations show T_e values of 1.26, 1.32, and 1.28 eV at $F(CH_4)=0$, 5, and 25 SCCM, respectively. As Figs. 3(b) and 5(b) show, such small changes in T_e can cause significant variations in the intensities of emissions from species like H ($n>2$) or Ar ($4p$), which are formed by electron impact excitation but, as we now show, the effect of such changes on the $I(H_\beta)/I(H_\alpha)$ ratio will be small. This ratio can be approximated as

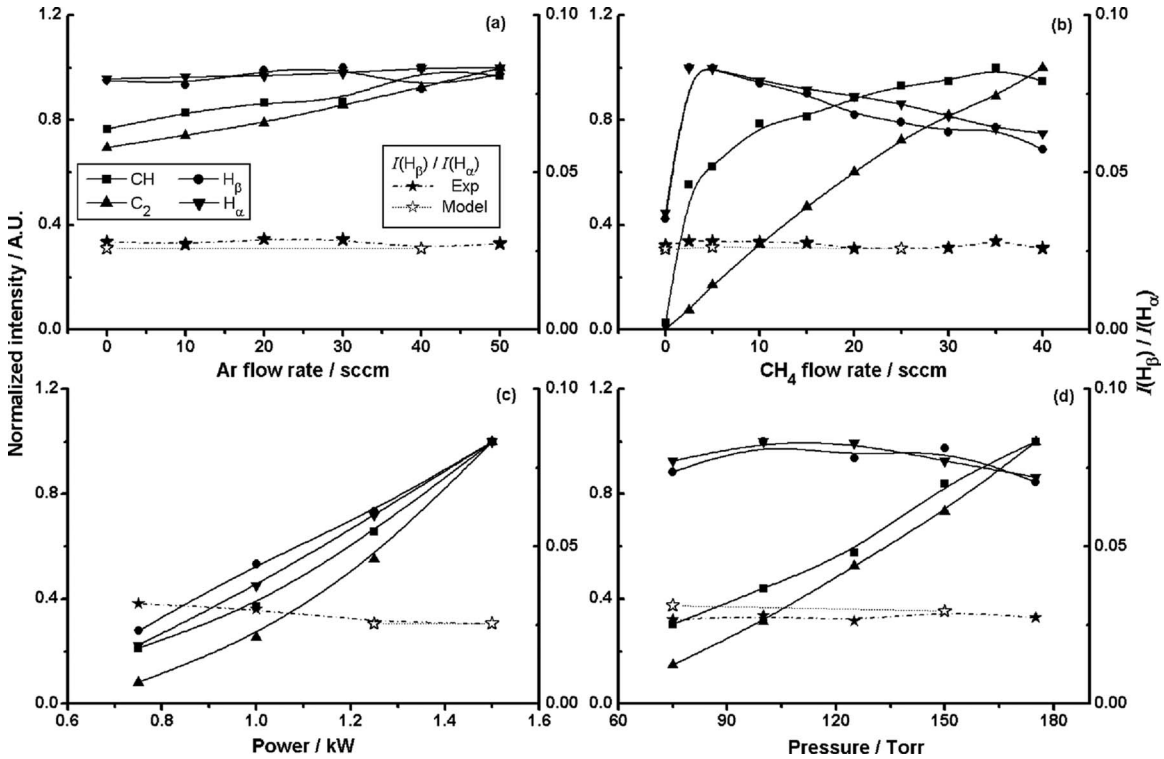

FIG. 5. Normalized relative H_α, H_β, $C_2(d-a)$, and $CH(A-X)$ emission intensities (left hand axis) and the relative intensity ratio $I(H_\beta)/I(H_\alpha)$ (right hand axis) plotted as functions of (a) $F(Ar)$, (b) $F(CH_4)$, (c) P, and (d) p. As in Fig. 3, the uncertainties in the normalized emission intensities from one spectrum to another recorded under the same process conditions are smaller than the displayed data points.

$$I(H_\beta)/I(H_\alpha) \sim \exp(-\Delta E/kT_e), \quad (4)$$

with $\Delta E \sim 0.65$ eV, the energy difference between the H ($n=4$) and H ($n=3$) levels. Given Eq. (4), the calculated changes in T_e upon adding, respectively, $F(CH_4)=5$ and 25 SCCM would result in increases in the $I(H_\beta)/I(H_\alpha)$ ratio of $\sim 2.3\%$ and $\sim 0.8\%$ only. Such small changes are within the noise associated with the present OES measurements.

The normalized $C_2(d)$ and $CH(A)$ emissions both increase with increasing $F(CH_4)$ but exhibit different behaviors. The former is seen to increase roughly linearly with $F(CH_4)$, whereas the CH emissions rise more steeply at low $F(CH_4)$ and then appear to "saturate" at higher CH_4 flow rates. Such trends mimic those observed in CRDS studies of $C_2(a)$ and $CH(X)$ radical column densities in this same reactor[10] and, as in that case, can be explained by differences in the thermal chemistry underpinning the formation and equilibration of these two radical species.[11]

The measured P-dependences of the various species emission intensities and the $I(H_\beta)/I(H_\alpha)$ ratio are displayed in Fig. 5(c). Both H Balmer emissions and the C_2 and CH radical emissions all increase rapidly with increasing input power. This can be understood by recognizing that increasing P leads to increases in both the H ($n=1$) density [see Fig. 3(c)] and in n_e, both of which are beneficial to forming H ($n>1$) atoms, and C_2 and CH radicals. The data shown in Fig. 5(c) hint at a modest drop in $I(H_\beta)/I(H_\alpha)$ ratio over the range $0.75 \leq P \leq 1.5$ kW. In the light of the earlier discussion, even a modest drop in $I(H_\beta)/I(H_\alpha)$ ratio such as shown here would require a significant fall in T_e. In reality, however, experiment [e.g., the evident increase in Ar ($4p$) and H_α emissions upon increasing P (Fig. 3(c))] and the 2D model calculations both indicate a modest increase in T_e over this range; the apparent drop is more likely a consequence of the weakness of the H_β emission intensities [and consequently larger uncertainty in $I(H_\beta)/I(H_\alpha)$ ratio] at low P.

Figure 5(d) shows the variation in normalized species emissions and $I(H_\beta)/I(H_\alpha)$ ratio as a function of total pressure. The $C_2(d)$ and $CH(A)$ emissions both increase with p, reflecting the thermally driven origin of the $C_2(a)$ and $CH(X)$ radicals from which they derive. The two H Balmer emissions exhibit very similar behaviors, maximizing at $p \sim 100-120$ Torr—for reasons discussed earlier [see Fig. 3(d)]. The $I(H_\beta)/I(H_\alpha)$ ratio is essentially constant across the range $75 < p < 175$ Torr. The model calculation shows that T_e falls, from 1.44 to 1.28 eV, when p is increased from 75 to 150 Torr, however. In addition, as discussed previously, the drop in the accompanying Ar ($4p$) emission [see Fig. 3(d)] also indicates that T_e must decline as a result of increasing p. The near constancy of the $I(H_\beta)/I(H_\alpha)$ value across this wide range of p again indicates that this ratio is not a sensitive indicator of T_e under the present experimental conditions. Nonetheless, it is worth re-emphasizing that while small changes in T_e may have relatively little effect on the $I(H_\beta)/I(H_\alpha)$ ratio, such electron characteristics do have a much more obvious effect on the absolute densities of the H ($n>1$) [and Ar ($4p$)] species (and thus on their respective emission intensities). Figure 5 also illustrates the good agreement between the $I(H_\beta)/I(H_\alpha)$ ratio calculated by inserting the predicted T_e value into Eq. (4) and then scaling by the appropriate factor.

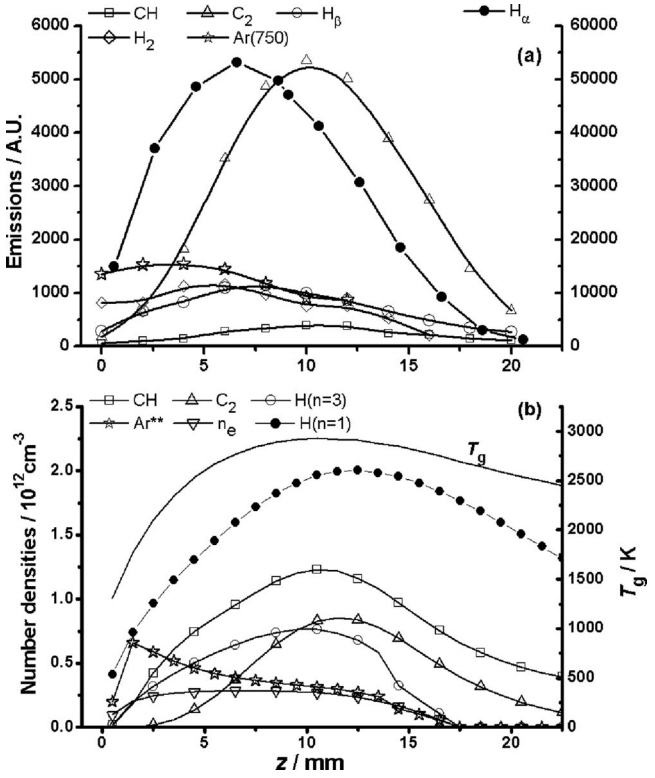

FIG. 6. (a) Measured emission intensities of Ar (750 nm), H_α, H_β, $H_2(3p, {}^3\Sigma_u^+)$, $C_2(d)$, and $CH(A)$ and (b) calculated number densities (at $r=0$ mm) of Ar^{**} [i.e., the Ar ($4s$) resonant states], H ($n=1$), H ($n=3$), C_2, CH, n_e, and T_{gas} from the 2D model (Ref. 11) plotted as functions of distance z above the substrate under base conditions. The number densities of Ar^{**}, H ($n=1$), and H ($n=3$) have been scaled by respective factors of 10^4, 5×10^{-5}, and 10^5 for ease of depiction in (b).

D. Emission profiles

Figure 6 compares the measured and predicted spatial profiles of various of the key excited state species. Emission profiles for Ar (750.4 nm), H_α, H_β, H_2, $C_2(d)$, and $CH(A)$ species obtained by spatially resolved OES are shown in Fig. 6(a), while Fig. 6(b) displays the Ar^{**} [i.e., Ar ($4s$) resonant states], H ($n=1$), H ($n=3$), $CH(X)$, and $C_2(a)$ number density profiles (at $r=0$ mm) predicted by the 2D modeling described in Ref. 11. Experimentally, the Ar (750.4 nm) and H_2 emission profiles are found to peak closest to the substrate, with the H_α and H_β emission intensities peaking at intermediate z and the C_2 and CH emissions maximizing at yet larger z (~ 10 mm). These trends are reproduced, qualitatively at least, by the modeling. The calculated n_e and T_{gas} versus z profiles are also included in Fig. 6(b). The T_{gas} profile peaks at very similar z to the calculated C_2 and CH density profiles (and their observed emission profiles), reinforcing the view that the distributions of these radical species are largely determined by thermal chemistry. The calculated H ($n=1$) profile extends to large z, but the calculated n_e profile falls quite rapidly once $z>10$ mm above the substrate. The dominant formation route for Ar^{**} and H ($n=3$) atoms is electron impact excitation of the respective ground state species (Table III). Thus the spatial profiles of these

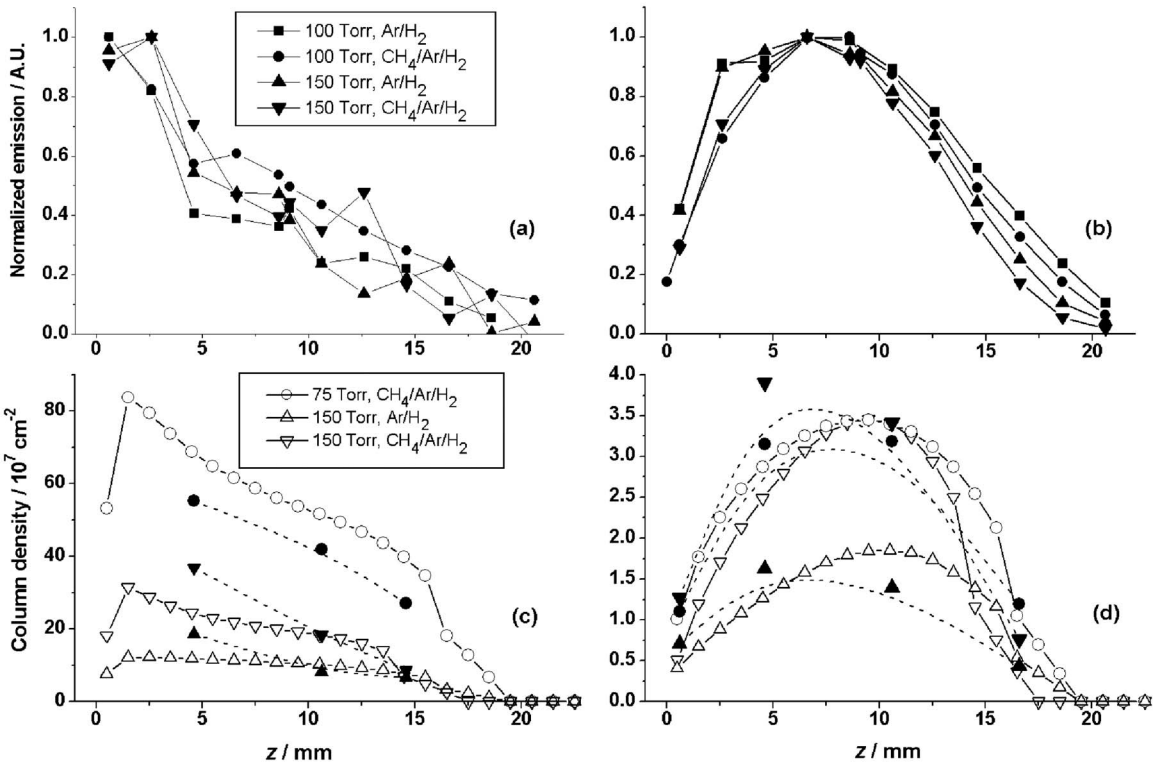

FIG. 7. Spatially resolved profiles of (a) Ar (750 nm) and (b) H_α emissions measured for Ar/H_2 ($p=100$, 150 Torr) and $CH_4/Ar/H_2$ [$p=100$, 150 Torr, $F(CH_4)=25$ SCCM] gas mixtures with, in each case, $F(Ar)=40$ SCCM, $F_{total}=565$ SCCM, and $P=1.5$ kW. Each of these profiles has been normalized so that the peak intensity is unity. As in Fig. 5, uncertainties in the normalized H_α emissions are smaller than the displayed data points, but the weakness of the Ar (750 nm) emissions means that the associated uncertainties at large z are as much as 10%. The lower panels show column density profiles of (c) Ar^{**} and (d) H ($n=3$) for Ar/H_2 ($p=75$ Torr) and $CH_4/Ar/H_2$ [$p=75$, 150 Torr, $F(CH_4)=25$ SCCM], returned by the 2D modeling with $F(Ar)=40$ SCCM, $F_{total}=565$ SCCM, and $P=1.5$ kW in each case. Superimposed on (c) and (d) are the Ar (750 nm) and H_α emission intensities measured under constant conditions (i.e., same optical configuration and CCD exposure time) for Ar/H_2 ($p=150$ Torr), (--▲--) and $CH_4/Ar/H_2$ [$p=100$, 150 Torr, $F(CH_4)=25$ SCCM] (--●-- and --▼--) plasmas. To aid comparison, the emission intensity data in panels (c) and (d) have been scaled vertically by appropriate factors so that the respective measured relative emission intensities match the predicted column density at $z=10.5$ mm and base process conditions.

excited state species are necessarily heavily influenced by the n_e distribution—as evidenced by the rapid declines in the predicted densities of both excited species in the $z=10-18$ mm region [Fig. 6(b)]. In principle, therefore, either the Ar ($4p$) or the H ($n=3$) emission profiles could be expected to provide a reliable estimate of the plasma size. In practice, however, the Ar ($4p$) emission is much weaker than the H_α emission under the present experimental conditions and, consistent with previous studies,[27–30] we conclude that the H_α emission profile provides the best indicator of the n_e distribution, its spatial extent, and thus the effective plasma volume. Nonetheless, careful inspection of Fig. 6(b) reveals that the Ar^{**} and H ($n=3$) densities both show significantly different z-dependences to n_e near the substrate ($z<10$ mm). The H ($n=3$) profile is most dependent on, and therefore appears to track, the H ($n=1$) distribution in this region. The Ar^{**} profile, in contrast, is much more sensitive to the steep fall in T_{gas} near the substrate, as a result of which the total gas density and the Ar mole fraction (due to thermodiffusion) increase rapidly as $z\rightarrow 0$. Thus the Ar^{**} density is predicted to peak at smaller z than either the n_e or H ($n=3$) distributions.

Figures 7(a) and 7(b) show the ways in which the measured Ar ($4p$) and H_α emission profiles vary with p and $F(CH_4)$. In order to highlight the different widths in these profiles, each has been scaled to the same peak intensity. Figures 7(c) and 7(d) show the corresponding Ar^{**} and H ($n=3$) column density profiles predicted by the 2D modeling, and their variation with p and $F(CH_4)$ (open symbols and solid curves). Superimposed on these latter figures are the measured Ar ($4p$) and H_α emissions (filled symbols and dashed curves), which have all been placed on a common relative scale by matching the predicted column density and the measured emission intensities at $z=10.5$ mm and base reactor conditions. Clearly, the 2D modeling reproduces the observed process dependent trends in the Ar ($4p$) and H ($n=3$) densities although, as in the companion CRDS study,[10] we note that the measured H ($n=3$) density appears to peak at smaller z than the model prediction—reflecting the form of the T_e versus z function assumed in the modeling.

The Ar ($4p$) emissions are relatively weak. The profiles shown in Fig. 7(a) all peak at small z, but any differences in the fine detail within them is lost in the poor signal to noise. The 2D modeling shows that the Ar^{**} density declines upon increasing p. CH_4 addition to an existing Ar/H_2 plasma is predicted to increase the density of Ar^{**} species, but to decrease their spatial extent. Such trends are mimicked by the measured Ar ($4p$) emission intensities [Fig. 7(c)]. The H_α emissions are much more intense (Fig. 2), and the measured profiles [Fig. 7(b)] show reproducible trends. All are asym-

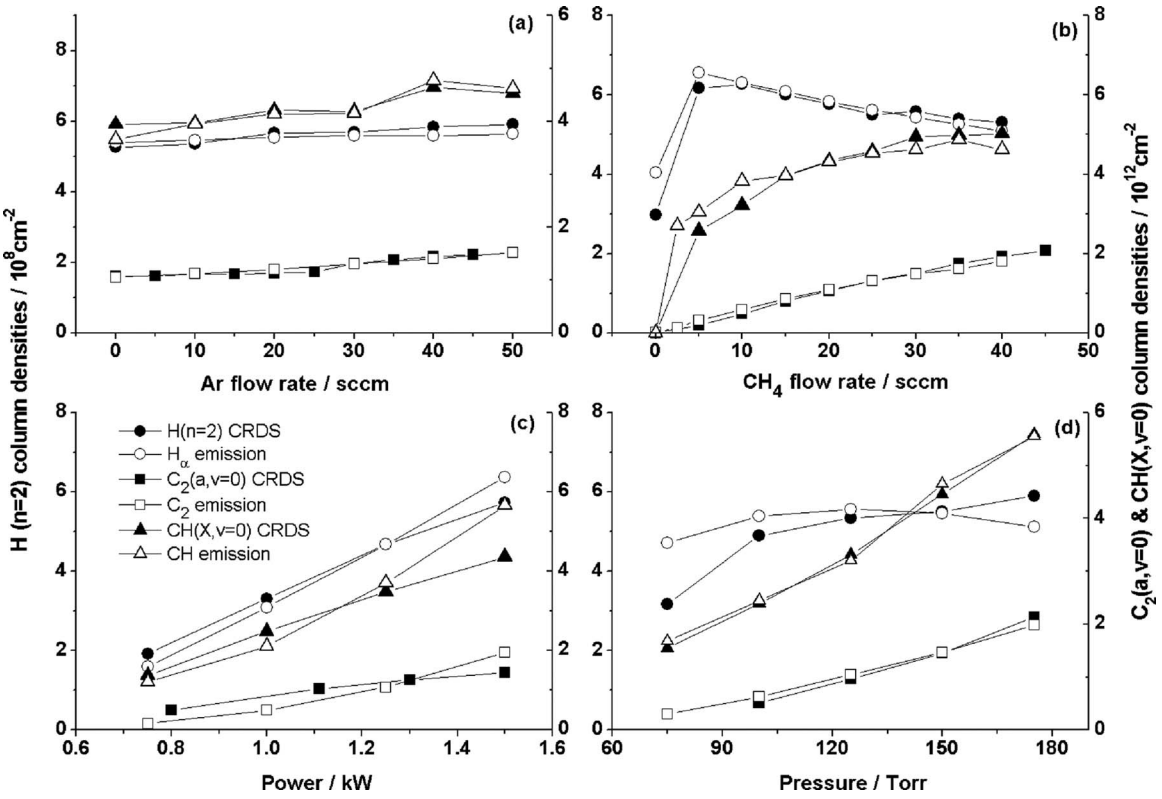

FIG. 8. Comparison of the H_α, $C_2(d)$, and $CH(A)$ emission intensities measured by OES and the absolute column densities of H $(n=2)$, $C_2(a,v=0)$, and $CH(X,v=0)$ measured by CRDS as functions of (a) $F(Ar)$, (b) $F(CH_4)$, (c) P, and (d) p. In each case, the OES data have been scaled by an appropriate factor to highlight the similarities between the two groups of data.

metric, declining more steeply at small z. This reflects the significant loss of H atoms and electrons at the substrate surface. Reducing p from 150 to 100 Torr results in a discernible expansion of the normalized H_α emission profile at large z in both cases [i.e., for $F(CH_4)=0$ and 25 SCCM]—consistent with the trends in H $(n=3)$ column density returned by the 2D modeling [Fig. 7(d)]. Introducing $F(CH_4)=25$ SCCM causes an obvious contraction of the normalized H_α emission profile at both small and large z, at both pressures studied. As discussed previously, the H_α emission profile at large z provides a good estimator of the plasma size and its variation with process conditions. The present data thus serve to reinforce the view that both increasing p and the addition of CH_4 into an Ar/H_2 plasma will tend to reduce the plasma volume (both its height and its radius, r_{pl}), consistent with the superposed experimental data points in Fig. 7(d) and the discussion accompanying Fig. 3(b). These trends reflect changes in both the electron characteristics and the thermal chemistry, as discussed previously in the context of Fig. 3. The absolute values of n_e and the Ar^{**} densities for three sets of process conditions shown in Figs. 7(c) and 7(d) follow the electron temperatures: $T_e \sim 1.26$ eV $[F(CH_4)=0$, $p=150$ Torr, $r_{pl}=3.4$ cm], $T_e \sim 1.28$ eV $[F(CH_4)=25$ SCCM, $p=150$ Torr, $r_{pl}=2.9$ cm], and $T_e \sim 1.44$ eV $[F(CH_4)=25$ SCCM, $p=75$ Torr, $r_{pl}=3.2$ cm]. The H $(n=3)$ number densities and spatial profiles depend not only on T_e and n_e but also on the H $(n=1)$ profiles. The H $(n=1)$ densities are determined by T_{gas}, which peaks in the plasma center and is calculated to span the range $T_{gas} \sim 2835$ K $[F(CH_4)=0$, $p=150$ Torr], ~ 2926 K $[F(CH_4)=25$ SCCM, $p=150$ Torr], and ~ 2830 K $[F(CH_4)=25$ SCCM, $p=75$ Torr] with these changes in process conditions. Other minor variations between the various profiles of any given species, and their sensitivity to process conditions, most probably reflect the pressure dependence of the diffusion coefficients.

E. Comparisons between species densities measured by OES and CRDS

Figure 8 compares the H_α, $C_2(d)$, and $CH(A)$ emission intensities measured using optical fiber 1 with the absolute column densities of H $(n=2)$ atoms and $C_2(a,v=0)$ and $CH(X,v=0)$ radicals measured by CRDS at $z=9.8$ mm,[10] as functions of the same four process parameters as considered in Figs. 3 and 5. In each case, the OES intensities for a given species have been scaled by an appropriate factor in order to emphasize similarities in the OES and CRDS measurements. In almost all cases, trends revealed by the OES data (which provides a relative measure of a local excited state number density) are quantitatively similar to those determined by CRDS [which provides an absolute measure of the column density of a low lying (or ground) state]. Thus, for example, the OES measurements successfully capture the comparative insensitivity of all three species to changes in $F(Ar)$ [Fig. 8(a)], the jump in H^* density upon adding $F(CH_4)=5$ SCCM, and the different dependences of the CH and C_2 radical densities with increasing $F(CH_4)$ [Fig. 8(b)]. However, each of the emission intensities shows a somewhat steeper P-dependence than the corresponding column densi-

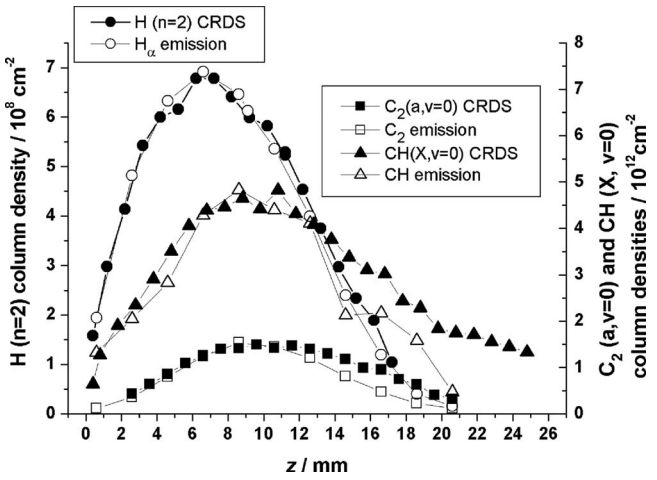

FIG. 9. Comparison of the OES measured H_α, $C_2(d)$, and CH(A) emission profiles with the column density profiles of H ($n=2$), $C_2(a,v=0)$, and CH($X,v=0$) measured by CRDS under base conditions. Each set of OES data has been scaled by an appropriate factor to emphasize the similar spatial dependences revealed by OES and CRDS.

ties measured by CRDS [Fig. 8(c)]. This reflects the fact that increasing P causes an increase not just in the C_2 and CH concentrations but also in n_e—which serves to boost the steady state density of each of the excited state species. Figure 8(d) reveals another point of difference: the H_α emission intensities and H ($n=2$) column densities show noticeably different p-dependences. This discrepancy likely reflects differences in the radiative loss channels available to H ($n=2$) and H ($n=3$) atoms. The Lyman transitions, $H(n=2)\rightarrow H(n=1)+h\nu$ and $H(n=3)\rightarrow H(n=1)+h\nu$, will both be optically thick under the present experimental conditions and the extent of reabsorption on such emissions will increase with p because of the p-dependence on the H ($n=1$) density [recall Fig. 3(d)]. But, unlike H ($n=2$), H ($n=3$) atoms can also decay via another (optically thin) radiative decay pathway: $H(n=3)\rightarrow H(n=2)+h\nu$. The availability of this process must reduce the p-dependence of the total quenching rate for H ($n=3$) atoms and may explain the different pressure dependences of the H ($n=3$) emissions and H ($n=2$) absorptions shown in Fig. 8(d).

Figure 9 compares the spatially resolved profiles of the H_α, CH (431 nm), and C_2 (516 nm) emission intensities with the CRDS measured column density profiles of H ($n=2$) atoms and CH (X, $v=0$) and $C_2(a,v=0)$ radicals in a $CH_4/Ar/H_2$ plasma operating at the base conditions. As in Fig. 8, the OES data have each been scaled by an appropriate factor to highlight the very similar z-dependences returned by the OES and CRDS measurements. The H_α spatial profile reproduces the z-dependence of the H ($n=2$) column density particularly well. This likely reflects the similar sources of the H ($n=3$) (responsible for the H_α emission) and H ($n=2$) atoms—i.e., the dominant formation route in both cases is electron impact excitation of the H ($n=1$) atoms, and the fact that the regions containing significant H ($n>1$) density and significant n_e are similar—as confirmed by the 2D model results.[11]

The situation regarding the axial profiles of C_2 and CH radicals and n_e is somewhat different, since both radicals exhibit significant density at z values where n_e is starting to fall quite rapidly.[11] This fact is significant when it comes to comparing the OES and CRDS profiles, since the two techniques monitor different species. OES measures species in excited electronic states [i.e., the $d\,^3\Pi_g$ state in the case of C_2, lying at $E=2.41$ eV above the ground state, and the $A\,^2\Delta$ state of CH ($E=2.88$ eV)], while CRDS samples population of the lower states [the $a\,^3\Pi_u$ state of C_2 ($E=0.09$ eV) and the ground state of CH]. Population of the lower states is determined by thermal chemistry, whereas formation of the excited state radicals requires not just the relevant lower state population but also electrons to promote the necessary excitation: the excited state radical densities are thus sensitive to both the thermal chemistry and the electron characteristics. Thus, the C_2 and CH emission profiles (which depend on the respective excited state densities and are proportional to the respective products $n_e\cdot[C_2]$ and $n_e\cdot[CH]$) start to appear truncated once $z>12$ mm in comparison with the $C_2(a)$ and CH(X) profiles. Indeed, as Fig. 9 shows, the C_2 and CH emission profiles only match the corresponding absorption profiles (from CRDS) at small z; in both cases, the emission profiles fall faster than the profiles returned by the CRDS measurements once z exceeds ~ 12 mm.

IV. CONCLUSIONS

OES has been used to explore further aspects of the plasma chemistry prevailing in a MWCVD reactor during growth of diamond under conditions of relatively high power ($P\leq 1.5$ kW) and pressure ($p\leq 175$ Torr). Relative densities of H ($n=1$) atoms are determined by actinometry, and the validity of using this method under the prevailing experimental conditions is discussed. The measured data confirm that H_2 dissociation under the present experimental conditions is largely thermal in origin. Excited species such as Ar ($4p$), $H_2(3p,{}^3\Sigma_u^+)$, $C_2(d)$, CH(A), and H ($n=3$) have also been investigated using OES to monitor specific emissions as functions of a set of discharge parameters [F(Ar), $F(CH_4)$, power, and pressure]. The monitored species subdivide into two groups according to the chemistry underpinning their generation: the production of species such as Ar ($4p$), $H_2(3p,{}^3\Sigma_u^+)$, and H ($n=2,3$) atoms is attributable to electron dominated chemistry, while other species such as C_2 and CH exhibit behavior characteristic of thermally driven chemistry. These two families exhibit quite different trends with respect to the various discharge parameters.

Spatially resolved measurements of the various emitting species are compared with the results of 2D reactor modeling calculations. Such comparisons confirm that the H_α emission profiles provide the best visualization of the n_e distribution (i.e., the plasma size). The Ar ($4p$) densities are heavily influenced by thermal diffusion effects and the resulting emissions thus peak much closer to the substrate. The OES measurements of electronically excited H ($n=3$), $C_2(d)$, and CH(A) species have also been compared with complementary H ($n=2$), $C_2(a)$, and CH(X) column density measurements (by CRDS) in this same reactor, and shown to be in very good agreement. Notwithstanding the recognized limitations of OES as a method for extracting information about

ground state species, the present studies show that careful OES measurements can offer a relatively straightforward and low cost route to future monitoring of diamond depositing plasmas under conditions such as those typically used for growth of polycrystalline (and single crystal) diamond.

ACKNOWLEDGMENTS

The Bristol group is grateful to EPSRC for the award of a portfolio grant GR/S71750/01 (LASER), to Element Six Ltd. for financial support and the long term loan of the MW reactor, to the University of Bristol and the Overseas Research Scholarship (ORS) scheme for a postgraduate scholarship (J.M.), and to colleagues K. N. Rosser and Dr. J. A. Smith for their many contributions to the work described here. Yu.A.M. acknowledges support from RF Government for Key Science Schools Grant No. 133.2008.2. The Bristol-Moscow collaboration is supported by a Royal Society Joint Project Grant.

APPENDIX: VALIDITY OF H ACTINOMETRY UNDER HIGH POWER AND HIGH PRESSURE CONDITIONS

Balancing the production and loss equations for H ($n=3$) atoms using the simplified reaction scheme listed in Table I, the H_α emission intensity can be written as

$$I_{H_\alpha} = K(\nu_{H_\alpha})\nu_{H_\alpha}A_{32}V_{emiss}\frac{[H(n=1)]K_e^{H_\alpha}n_e}{[H]K_{QH}^{H_\alpha}+[H_2]K_{QH_2}^{H_\alpha}+K_R}$$
$$= [K(\nu_{H_\alpha})\nu_{H_\alpha}A_{32}V_{emiss}/K_R]\times\frac{[H(n=1)]K_e^{H_\alpha}n_e}{[H](K_{QH}^{H_\alpha}/K_R)+[H_2](K_{QH_2}^{H_\alpha}/K_R)+1}, \quad (A1)$$

where $K(\nu_{H_\alpha})$ is the detection response coefficient at 656.5 nm, ν_{H_α} is the H_α transition frequency, V_{emiss} is the emission volume, $K_{QH}^{H_\alpha}$ and $K_{QH_2}^{H_\alpha}$ are the respective quenching rates for H ($n=3$) atoms in collision with H and H_2, and K_R is the radiative decay rate:[26]

$$K_R = A_{32}+A_{31} = (4.36+5.39)\times 10^7\ \ s^{-1} = 9.8\times 10^7\ \ s^{-1}. \quad (A2)$$

The Ar ($4p$) emission intensity can similarly be written as

$$I_{Ar^*} = [K(\nu_{Ar^*})\nu_{Ar^*}A_{44}V_{emiss}/K_{RAr}]\times\frac{[Ar(3p)]K_e^{Ar^*}n_e}{[H](K_{QH}^{Ar^*}/K_{RAr})+[H_2](K_{QH_2}^{Ar^*}/K_{RAr})+1}. \quad (A3)$$

Recognizing that

$$K_{RAr} = A_{44}, \quad (A4)$$

the $H(n=1):Ar(3p)$ ratio can be written as

$$\frac{[H(n=1)]}{[Ar(3p)]} = F\frac{K_e^{Ar^*}}{K_e^{H_\alpha}}Q_T\frac{I_{H_\alpha}}{I_{Ar^*}}, \quad (A5)$$

where

$$F = \frac{K(\nu_{Ar^*})}{K(\nu_{H_\alpha})}\frac{\nu_{H_\alpha}}{\nu_{Ar^*}}\frac{A_{32}+A_{31}}{A_{32}} \quad (A6)$$

is a constant.

$K_e^{Ar^*}/K_e^{H_\alpha}$ is only weakly dependent on T_e, due to the similar threshold and electron impact excitation cross section versus T_e-dependences for forming Ar ($4p$) and H ($n=3$) atoms.[26] Provided T_e is relatively insensitive to changes in process conditions within the experiment, $K_e^{Ar^*}/K_e^{H_\alpha}$ can also be treated as a constant. Thus, the only term likely to show a significant pressure and temperature dependence is

$$Q_T = \frac{[H](K_{QH}^{H_\alpha}/K_R)+[H_2]((K_{QH_2}^{H_\alpha}/K_R)+1}{[H](K_{QH}^{Ar^*}/K_{RAr})+[H_2]((K_{QH_2}^{Ar^*}/K_{RAr})+1}. \quad (A7)$$

$[H_2]K_{QH_2}^{Ar^*}$ and $[H]K_{QH}^{Ar^*}$ can be written as, respectively,

$$[H_2]K_{QH_2}^{Ar^*} = (p/RT)v_{Ar-H_2}\sigma_{Ar^*-H_2}x_{H_2}, \quad (A8)$$

$$[H]K_{QH}^{Ar^*} = (p/RT)v_{Ar}\sigma_{Ar^*-H}x_H, \quad (A9)$$

where v_{Ar-H_2} and v_{Ar-H} are the mean velocity of Ar relative to H_2 and H, respectively, $\sigma_{Ar^*-H_2}$ and σ_{Ar^*-H} are the associated quenching cross sections with H_2 and H, and x_{H_2} and x_H are the H_2 and H atom mole fractions. Similar equations can be written for $[H_2]K_{QH_2}^{H_\alpha}$ and $[H]K_{QH}^{H_\alpha}$.

Given the cross sections (in Å^2), gas temperature (in K), and pressure (in Torr), and following Ref. 26, Q_T can be written as

$$Q_T = \frac{1+pT^{-1/2}(0.176\sigma_{H_\alpha-H_2}x_{H_2}+0.202\sigma_{H_\alpha-H}x_H)}{1+pT^{-1/2}(0.215\sigma_{Ar^*-H_2}x_{H_2}+0.301\sigma_{Ar^*-H}x_H)}. \quad (A10)$$

Inserting the values for these respective cross sections adopted by Gicquel *et al.*,[5] i.e., $\sigma_{H_\alpha-H}=46.2$ Å^2, $\sigma_{Ar^*-H}=53$ Å^2, $\sigma_{H_\alpha-H_2}=62$ Å^2 (the average of the values 58 and 65 Å^2 found in Refs. 31 and 32, respectively), and $\sigma_{Ar^*-H_2}=65$ Å^2, Eq. (A10) reduces to

$$Q_T = \frac{1+pT^{-1/2}(10.912x_{H_2}+9.332x_H)}{1+pT^{-1/2}(13.975x_{H_2}+15.953x_H)}. \quad (A11)$$

The 2D modeling[11] shows that $x_{H_2} \gg x_H$, i.e., that the degree of H_2 dissociation is small (typically ~4%, recall Fig. 3), so Eq. (A11) can be further simplified to

$$Q_T = \frac{1+pT^{-1/2}(10.912x_{H_2})}{1+pT^{-1/2}(13.975x_{H_2})}. \quad (A12)$$

The present experiments involve pressures in the range $75 \le p \le 175$ Torr and gas temperatures (in the plasma region) in the range 2500–3200 K, ensuring that

$$pT^{-1/2}(10.912x_{H_2}) \gg 1 \quad (A13)$$

at all times and that Q_T is effectively a constant. Thus all of the terms preceding the intensity ratio in Eq. (A5) are constants—as required in order that the validity conditions

for use of actinometry in the present experiments are satisfied.

[1]W. Zhu, A. Inspektor, A. R. Badzian, T. McKenna, and R. Messier, J. Appl. Phys. **68**, 1489 (1990).
[2]A. Gicquel, K. Hassouni, Y. Breton, M. Chenevier, and J. C. Cubertafon, Diamond Relat. Mater. **5**, 366 (1996).
[3]A. Gicquel, M. Chenevier, Y. Breton, M. Petiau, J. P. Booth, and K. Hassouni, J. Phys. III **6**, 1167 (1996).
[4]A. Gicquel, K. Hassouni, S. Farhat, Y. Breton, C. D. Scott, M. Lefebvre, and M. Pealat, Diamond Relat. Mater. **3**, 581 (1994).
[5]A. Gicquel, M. Chenevier, K. Hassouni, A. Tserepi, and M. Dubus, J. Appl. Phys. **83**, 7504 (1998).
[6]T. Lang, J. Stiegler, Y. von Kaenel, and E. Blank, Diamond Relat. Mater. **5**, 1171 (1996).
[7]A. N. Goyette, J. E. Lawler, L. W. Anderson, D. M. Gruen, T. G. McCauley, D. Zhou, and A. R. Krauss, Plasma Sources Sci. Technol. **7**, 149 (1998).
[8]P. John, J. R. Rabeau, and J. I. B. Wilson, Diamond Relat. Mater. **11**, 608 (2002).
[9]J. Ma, A. Cheesman, M. N. R. Ashfold, K. Hay, S. Wright, N. Langford, G. Duxbury, and Yu. A. Mankelevich, J. Appl. Phys. (submitted).
[10]J. Ma, J. C. Richley, M. N. R. Ashfold, and Yu. A. Mankelevich, J. Appl. Phys. **104**, 103305 (2008).
[11]Yu. A. Mankelevich, M. N. R. Ashfold, and J. Ma, J. Appl. Phys. **104**, 113304 (2008).
[12]A. Cheesman, J. A. Smith, M. N. R. Ashfold, N. Langford, S. Wright, and G. Duxbury, J. Phys. Chem. A **110**, 2821 (2006).
[13]J. Ma, Ph.D. thesis, University of Bristol, 2008.
[14]D. G. Goodwin and J. E. Butler, in *Handbook of Industrial Diamonds and Diamond Films*, edited by M. A. Prelas, G. Popovici, and L. K. Bigelow (Dekker, New York, 1998), pp. 527–581 (and references therein).
[15]M. N. R. Ashfold, P. W. May, J. R. Petherbridge, K. N. Rosser, J. A. Smith, Y. A. Mankelevich, and N. V. Suetin, Phys. Chem. Chem. Phys. **3**, 3471 (2001).
[16]F. G. Celii and J. E. Butler, Appl. Phys. Lett. **54**, 1031 (1989).
[17]S. A. Redman, C. Chung, K. N. Rosser, and M. N. R. Ashfold, Phys. Chem. Chem. Phys. **1**, 1415 (1999).
[18]U. Meier, K. Kohse-Hoinghaus, L. Schafer, and C.-P. Klages, Appl. Opt. **29**, 4993 (1990).
[19]J. P. Booth and N. Sadeghi, J. Appl. Phys. **70**, 611 (1991).
[20]L. Schafer, C.-P. Klages, U. Meier, and K. Kohse-Hoinghaus, Appl. Phys. Lett. **58**, 571 (1991).
[21]M. Chenevier, J. C. Cubertafon, A. Campargue, and J. P. Booth, Diamond Relat. Mater. **3**, 587 (1994).
[22]J. W. Coburn and M. Chen, J. Appl. Phys. **51**, 3134 (1980).
[23]A. Rousseau, A. Granier, G. Gousset, and P. Leprince, J. Phys. D **27**, 1412 (1994).
[24]Z.-C. Geng, Y. Xu, X.-F. Yang, W. G. Wang, and A. M. Zhu, Plasma Sources Sci. Technol. **14**, 76 (2005).
[25]M. Abdel-Rahman, V. Schulz-von der Gathen, T. Gans, K. Niemi, and H. F. Doebele, Plasma Sources Sci. Technol. **15**, 620 (2006).
[26]A. Gicquel, M. Chenevier, and M. Lefebvre, in *Handbook of Industrial Diamonds and Diamond Films*, edited by M. A. Prelas, G. Popovici, and L. K. Bigelow (Dekker, New York, 1998), pp. 739–796 (and references therein).
[27]K. Hassouni, T. A. Grotjohn, and A. Gicquel, J. Appl. Phys. **86**, 134 (1999).
[28]K. Hassouni, A. Gicquel, M. Capitelli, and J. Loureiro, Plasma Sources Sci. Technol. **8**, 494 (1999).
[29]K. Hassouni, O. Leroy, S. Farhat, and A. Gicquel, Plasma Chem. Plasma Process. **18**, 325 (1998).
[30]G. Lombardi, K. Hassouni, G.-D. Stancu, L. Mechold, J. Ropcke, and A. Gicquel, J. Appl. Phys. **98**, 053303 (2005).
[31]B. L. Preppernau, K. Pearce, A. Tserepi, E. Wurzburg, and T. A. Miller, Chem. Phys. **196**, 371 (1995).
[32]J. Bittner, K. Kohse-Hoinghaus, U. Meier, and T. Just, Chem. Phys. Lett. **143**, 571 (1988).